Supplementary Information

Practical wavelength selection for quantum-augmented networks over shared optical fiber

Nitin Jha, Prateek Paudel and Abhishek Parakh

Kennesaw State University, GA, USA

Appendix labels, equation numbers and citation numbers follow the accompanying main manuscript. References to main-text equations, sections and figures refer to that manuscript.

A Optical-noise derivations

A.1 Raman Noise Model

The silica Raman response is described by the multiple-vibrational-mode model of Ref.,[24]

$$h_R(t) = \sum_{k=1}^{13} A_k \, e^{-\gamma_k t} \, e^{-\Gamma_k^2 t^2/4} \sin(\omega_k t), \qquad t \geq 0, \tag{60}$$

with $\omega_k = 2\pi c \tilde{\nu}_k$, $\Gamma_k = \pi c G_k$, and $\gamma_k = \pi c L_k$. The component positions $\tilde{\nu}_k$ and the Gaussian and Lorentzian widths G_k and L_k are tabulated in wavenumbers, whereas A_k are the relative amplitudes reported in that reference. The Raman gain spectrum is proportional to the imaginary part of the Fourier transform of h_R,

$$g_R(\Delta f) \propto \mathrm{Im} \int_0^\infty h_R(t) \, e^{i 2\pi \Delta f \, t} \, dt, \qquad \Delta f \geq 0, \tag{61}$$

and peaks at 13.2 THz (440 cm^{-1}).

The spontaneous coefficient carries the Bose–Einstein occupation $n_{\mathrm{th}}(\Delta f) = [\exp(h|\Delta f|/k_B T) - 1]^{-1}$ on each side,

$$\tilde{g}(\Delta f) = g_R(|\Delta f|) \times \begin{cases} n_{\mathrm{th}}(\Delta f) + 1, & \Delta f > 0 \text{ (Stokes)}, \\ n_{\mathrm{th}}(\Delta f), & \Delta f < 0 \text{ (anti-Stokes)}, \end{cases} \tag{62}$$

and its level is fixed at a measured point,

$$\rho_R(\Delta f) = \rho_0 \, \frac{\tilde{g}(\Delta f)}{\tilde{g}(\Delta f_0)}. \tag{63}$$

Here $\rho_0 = 2.85 \times 10^{-9} \, \mathrm{km}^{-1} \, \mathrm{nm}^{-1}$ is the coefficient measured in standard single-mode fiber at pump and observation wavelengths of 1559.79 and 1554.94 nm, $\Delta f_0 = -0.599$ THz.[25] It is converted to frequency units at the observation wavelength, $\rho_0^{(f)} = \rho_0 \, \lambda_{\mathrm{obs}}^2 / c = 2.30 \times 10^{-23} \, \mathrm{m}^{-1} \, \mathrm{Hz}^{-1}$. Following that source, we sum the coefficient over polarizations and apply the factor 1/2 in main-text Equation (38) once.

Spontaneous Raman noise in the same fiber type has also been measured directly at carrier offsets of 0.1–1.4 THz.[26] Using the average of the reported linear slopes, the measured coefficient at 0.6 THz is a factor of 4.3 below Equation (63). With both normalized at 0.6 THz, the model exceeds the measurement by a factor of 5.6 at 0.1 THz and falls below it by a factor of 2 at 1.4 THz, because the measured coefficient decreases linearly toward the carrier while the gain-derived spectrum is nearly flat there. The measured level is used as a sensitivity case, $\rho_R \to 0.235 \, \rho_R$.

Using the notation of Section 2 of the main manuscript, let $a_{c_i} = a(\lambda_{c_i})$, $a_f = a(c/f)$, and $\Delta f_{iq} = f_{c_i} - f_q$. The longitudinal coordinate z is measured from Alice toward Bob, and the classical power is

$$P_{c_i}^{(m)}(z) = P_{c_i}^{(m)}(0) e^{-a_{c_i} z}. \tag{64}$$

Evaluating the longitudinal integral in main-text Equation (17) at each optical frequency f gives

$$S_{\mathrm{R,out}}^{(m)}(f; f_q) = \eta_{\mathrm{rx},m} T_q(f; f_q) \sum_{i=1}^{N_c} P_{c_i}^{(m)}(0) \, \rho_R(f_{c_i} - f) \, \Lambda_i^{(m)}(f). \tag{65}$$

For co-propagation, reception occurs at Bob and $\ell_m(z) = L_m - z$, so that

$$\Lambda_i^{\mathrm{co},m}(f) = e^{-a_f L_m}\,\frac{1 - e^{-(a_{c_i} - a_f)L_m}}{a_{c_i} - a_f}. \tag{66}$$

When $a_{c_i} = a_f = a$, the continuous limit is

$$\Lambda_i^{\mathrm{co},m}(f) = L_m e^{-aL_m}. \tag{67}$$

For counter-propagation, reception occurs at Alice and $\ell_m(z) = z$. Consequently,

$$\Lambda_i^{\mathrm{counter},m}(f) = \frac{1 - e^{-(a_{c_i} + a_f)L_m}}{a_{c_i} + a_f}. \tag{68}$$

These closed forms are exact at each frequency. The numerical results integrate Equation (65) against the accepted mode through main-text Equation (38). When ρ_R and the attenuation vary negligibly across the accepted mode, the occupancy added by classical channel i during traversal m reduces to

$$\nu_{\mathrm{R},i}^{(m)} \simeq \frac{\eta_{\mathrm{rx},m} P_{c_i}^{(m)}(0)\,\rho_R(\Delta f_{iq})\,\Lambda_i^{(m)}(f_q)\,\eta_\psi(f_q)}{2hf_q}, \tag{69}$$

$$\eta_\psi(f_q) = \int |\psi_m(f)|^2 T_q(f; f_q)\,df. \tag{70}$$

so the background enters through the mode-weighted filter transmission η_ψ rather than through the filter bandwidth.

A.2 XPM phase variance

We assume the deterministic mean differential phase is compensated. Within the selected-mode approximation, the residual differential phase is constant over each quantum pulse. Define the retarded classical power fluctuation

$$\begin{aligned}\delta P_{i,m}(z,t) = {} & P_{c_i}^{(m)}\big(z, t - \tau_{iq}^{(m)}(z)\big) \\ & - \mathbb{E}\Big[P_{c_i}^{(m)}\big(z, t - \tau_{iq}^{(m)}(z)\big)\Big].\end{aligned} \tag{71}$$

The residual phase therefore satisfies

$$\delta\phi_m(t) = 2\sum_{i=1}^{N_c} \gamma_{iq}(\lambda_q)\kappa_{i,m} \int_0^{L_m} \delta P_{i,m}(z,t)\,dz. \tag{72}$$

Assume jointly stationary intensity fluctuations with finite second moments, and define

$$K_{ij}^{(m)}(z,z') = \mathbb{E}[\delta P_{i,m}(z,t)\delta P_{j,m}(z',t)]\,. \tag{73}$$

For stationary fluctuations, the covariance is independent of t. The residual phase has zero mean, so its variance follows by squaring and averaging Equation (72):

$$\begin{aligned}\sigma_{\phi,m}^2 &= \mathrm{Var}(\delta\phi_m(t)) \\ &= 4\sum_{i,j=1}^{N_c} \gamma_{iq}(\lambda_q)\gamma_{jq}(\lambda_q)\kappa_{i,m}\kappa_{j,m} \\ &\quad \times \int_0^{L_m}\int_0^{L_m} K_{ij}^{(m)}(z,z')\,dz\,dz'.\end{aligned} \tag{74}$$

For statistically independent intensity fluctuations on distinct classical channels, $K_{ij}^{(m)}(z,z') = 0$ when $i \neq j$. For the numerical results, each launched power fluctuation propagates with the loss of its channel and walks off from the quantum pulse at a constant rate, $\delta P_{i,m}(z,t) = e^{-a_{c_i} z}\,\delta P_i\big(t - d_i^{(m)} z\big)$, where δP_i is the fluctuation at the

launch plane, $d_i^{(m)} = |\beta_1(f_{c_i}) - \beta_1(f_q)|$ for co-propagation and $d_i^{(m)} = \beta_1(f_{c_i}) + \beta_1(f_q)$ for counter-propagation, and $\beta_1 = 1/v_g$ is the inverse group velocity. Then $K_{ii}^{(m)}(z, z') = e^{-a_{c_i}(z+z')} R_i\big(d_i^{(m)}(z-z')\big)$, with R_i the autocorrelation of δP_i, and Equation (74) becomes

$$\sigma_{\phi,m}^2 = 4 \sum_{i=1}^{N_c} \gamma_{iq}^2 \kappa_{i,m}^2 \int S_i(F) \left|H_i^{(m)}(F)\right|^2 dF, \qquad H_i^{(m)}(F) = \frac{1 - e^{-(a_{c_i} + i2\pi F d_i^{(m)}) L_m}}{a_{c_i} + i2\pi F d_i^{(m)}}, \tag{75}$$

where S_i is the two-sided power spectral density of δP_i. We take S_i flat, $S_i(F) = \sigma_{P,i}^2/(2B)$ for $|F| \le B$ and zero otherwise, with $\sigma_{P,i}$ set by a relative fluctuation depth of the launch power. The F integral then has a closed form in terms of the exponential integral, which is used numerically and checked against direct quadrature of Equations (74) and (75). This second-moment calculation does not by itself imply the Gaussian phase statistics assumed in Section 2 of the main manuscript. The covariance of residual XPM phases separated by a delay τ is

$$\Gamma_{\phi,m}(\tau) = 4 \sum_{i=1}^{N_c} \gamma_{iq}^2 \kappa_{i,m}^2 \int S_i(F) |H_i^{(m)}(F)|^2 \cos(2\pi F \tau)\, dF, \tag{76}$$

where $\Gamma_{\phi,m}(0) = \sigma_{\phi,m}^2$. Qubits arriving at times t_j and t_k have phase covariance $\Gamma_{\phi,m}(t_j - t_k)$. Under jointly Gaussian phase statistics, vanishing off-diagonal covariances imply independent phase errors. Any pulse schedule must also be checked for correlations across traversals and between accepted background modes.

A.3 Full-chain mode reference

The scalar composition in main-text Equation (39) assumes mode restoration between traversals. For comparison, we retain the frequency-dependent field transfer through the complete exchange, $t_{\mathrm{tot}}(f) = \prod_{m=1}^{3} t_m(f)$, and project the signal and background once at the final output:

$$\begin{aligned} T_{\mathrm{ref}} &= \left| \int \psi^*(f) t_{\mathrm{tot}}(f) \psi(f)\, df \right|^2, \\ \nu_{\mathrm{ref}} &= \sum_{m=1}^{3} \int |\psi(f)|^2 \Big[\prod_{l>m} |t_l(f)|^2 \Big] \frac{S_{\mathrm{add,out}}^{(m)}(f)}{2hf}\, df. \end{aligned} \tag{77}$$

The same ideal temporal alignment and propagation-phase matching are assumed. Unused input optical modes are in vacuum. Under the independent, stationary Gaussian background model, the selected final mode is a phase-insensitive Gaussian channel characterized by T_{ref} and ν_{ref}. These values can therefore be substituted into the accepted-channel formulas to calculate the reference certificate and yield. The comparison is evaluated at selected diagnostic candidates of the four operating points. Reported discrepancies are maxima over these candidates. The wavelength scans and operating maps retain the scalar composition.

Figure S1(a) compares the explicit three-traversal channel with its effective composition, with Choi-operator discrepancies below 10^{-15}. At the evaluated candidates of the four operating points, the full-chain reference differs from the scalar recurrence by at most 0.6% in T and 0.4% in ν. The resulting changes in $C_{7,1}$ and Y_{lb} are at most 1.2×10^{-3} and 4.5%, respectively (Figure S1(b)). Broader prescribed FWM profiles reduce the peak occupancy at all four operating points (Figure S1(c)).

A.4 Numerical configuration and sensitivity cases

The baseline settings are specified in `configs/illustrative_baseline.yaml` in the released repository. The sensitivity cases in main-text Figure 4(d) are defined in `scripts/run_sensitivity.py`. Shapes A and B use the `multi_gaussian_v1` and `damped_oscillator_v1` models, respectively, implemented in `src/raman.py`. Both use the same Bose conversion and normalization point as the baseline Raman model. They are assumed alternative shapes, not fits to measured spectra. The analytic attenuation case uses the three-term model in `src/attenuation.py`, anchored to 0.180 dB km^{-1} at 1550 nm. The receiver power-average case replaces the modal filter transmission in main-text Equation (11) with $\int |\psi_m(f)|^2 T_q(f; f_q)\, df$. The broadened FWM cases assign each generated component a normalized Gaussian profile with an rms width of 1, 5 or 25 GHz while keeping its total power fixed. These prescribed profiles test spectral overlap and do not simulate modulated FWM generation.

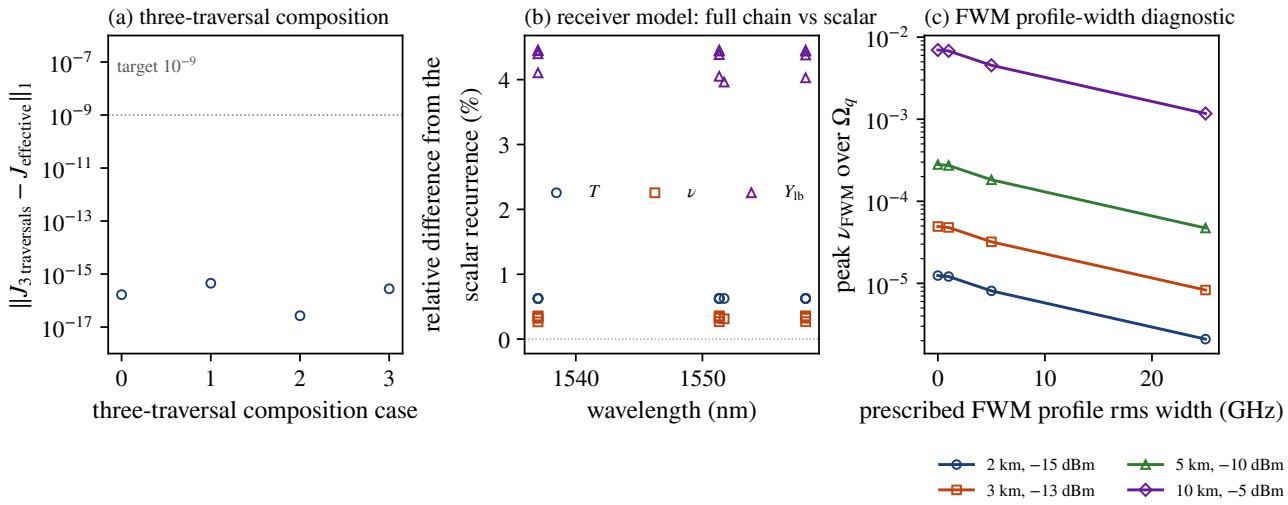

Figure S1: Numerical diagnostics. (a) Choi-operator discrepancy for three-traversal composition. (b) Relative differences in T, ν and Y_{lb} between the full-chain reference and scalar recurrence. (c) Peak summed per-traversal FWM occupancy, $\max_{\lambda\in\Omega_q^{\text{eval}}} \sum_{m=1}^{3} \nu_{\text{FWM},m}(\lambda)$, versus profile rms width.

B Accepted optical channel

Let $\mathcal{E}_{T,\nu}$ denote the phase-insensitive Gaussian channel with signal power transmissivity T and vacuum-input output occupancy ν. It has the representation[27]

$$\mathcal{E}_{T,\nu} = \mathcal{A}_G \circ \mathcal{L}_\zeta, \qquad G = 1+\nu, \qquad \zeta = \frac{T}{G}, \tag{78}$$

where $\mathcal{L}_\zeta$ is pure loss and $\mathcal{A}_G$ is a quantum-limited amplifier of power gain G. Their composition has signal transmissivity $G\zeta = T$ and vacuum-input occupancy $G-1=\nu$. For a beam-splitter dilation with $T<1$, the environment occupancy is $\nu/(1-T)$.

Write $\omega = W\rho W^\dagger$ and $|\text{vac}\rangle = |0_H, 0_V\rangle$. Applying pure loss independently to both polarizations gives

$$\mathcal{L}_\zeta^{\otimes 2}(\omega) = \zeta\omega + (1-\zeta)|\text{vac}\rangle\langle\text{vac}|\ \text{Tr}\,\rho. \tag{79}$$

The amplifier Kraus operators act on a Fock state as

$$K_\ell|p\rangle = \sqrt{\binom{p+\ell}{\ell}}\,\frac{(G-1)^{\ell/2}}{G^{(p+\ell+1)/2}}|p+\ell\rangle, \qquad p,\ell\geq 0, \tag{80}$$

with $G=1$ understood as the identity channel. For a one-photon input across both polarizations, only the branch adding no photons can contribute to the final one-photon subspace. Its amplitude is $G^{-3/2}$. For vacuum input, the probabilities of zero and one photon in either polarization are G^{-1} and $(G-1)G^{-2}$, respectively. Thus,

$$\begin{aligned}\Pi_1\mathcal{A}_G^{\otimes 2}(\omega)\Pi_1 &= G^{-3}\omega,\\ \Pi_1\mathcal{A}_G^{\otimes 2}(|\text{vac}\rangle\langle\text{vac}|)\Pi_1 &= \frac{G-1}{G^3}\Pi_1.\end{aligned} \tag{81}$$

Combining the loss and amplifier operations, then decoding with $W^\dagger$, gives

$$\begin{aligned}\mathcal{M}_{\text{opt}}(\rho) &= W^\dagger\Pi_1\mathcal{E}_{T,\nu}^{\otimes 2}(\omega)\Pi_1 W\\ &= \frac{\zeta}{G^3}\rho + \frac{(1-\zeta)(G-1)}{G^3}I_2\ \text{Tr}\,\rho\\ &= c_0\rho + c_1\frac{I_2}{2}\,\text{Tr}\,\rho,\end{aligned} \tag{82}$$

where

$$c_0 = \frac{T}{(1+\nu)^4}, \qquad c_1 = \frac{2\nu(1+\nu-T)}{(1+\nu)^4}. \tag{83}$$

Taking the trace gives

$$\operatorname{Tr}\mathcal{M}_{\mathrm{opt}}(\rho) = (c_0 + c_1)\operatorname{Tr}\rho. \tag{84}$$

Every normalized input polarization state therefore has acceptance probability $s = c_0 + c_1$. For $s > 0$, normalization gives $r = c_1/s$.

Equivalently, $\mathcal{M}^{\dagger}_{\mathrm{opt}}(I_2) = sI_2$. For n independent identical optical channels, the block-acceptance effect is $s^n I_{2^n}$. Hence $P_{\mathrm{acc}} = s^n$ also holds for entangled encoded inputs.

C Base-error limits and link-budget operation

Figure S2 reports the base-error limit $e_0^{\max}$ defined by the fidelity certificate in main-text Equation (58), over the distance–power grid (panel (a)) and along the classical link-budget minima (panel (b)). Published error levels are included for comparison. Panel (c) evaluates the optimized yield bound at $e_0 = 0.2\%$. Along the 1.25 Gb/s link budget, this bound falls below $Y_{\min} = 10^{-6}$ between 10 and 11 km per traversal, while fidelity remains certified at longer spans.

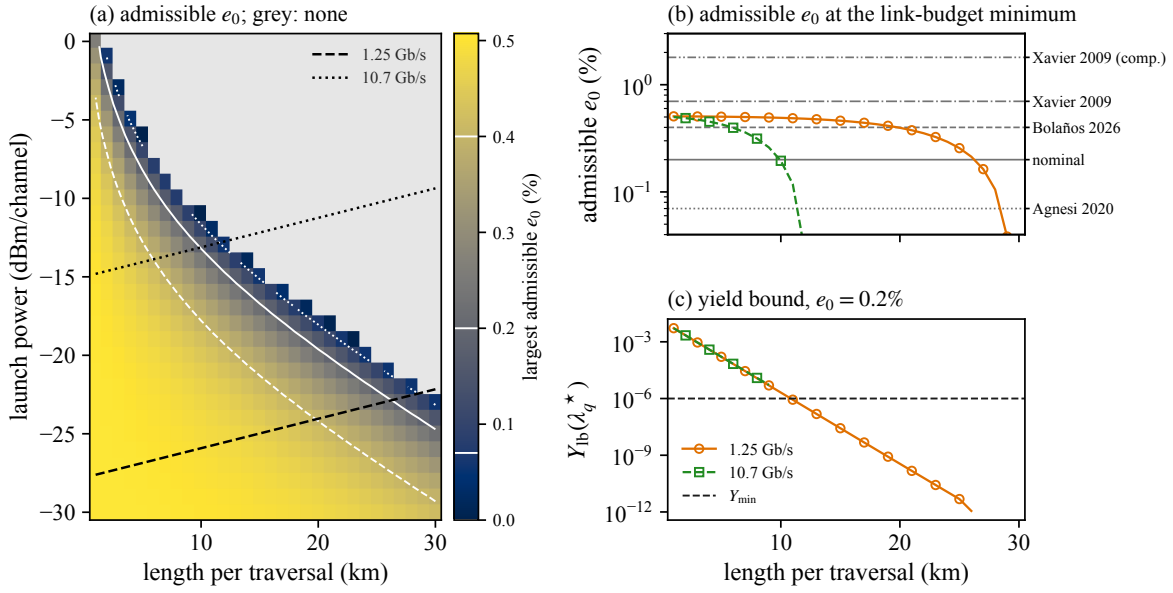

Figure S2: Base-error limits and classical link budgets. (a) Largest admissible base error over distance and launch power; grey indicates failure of certification at $e_0 = 0$. (b) Limits along the 1.25 and 10.7 Gb/s link-budget minima, with published comparison levels. (c) Optimized yield bound at $e_0 = 0.2\%$, with $Y_{\min} = 10^{-6}$. Xavier 2009 and Xavier 2009 (comp.) denote the static-fiber and active-compensation conditions of the same study.[30]

References

[24] Hollenbeck, D. & Cantrell, C. D. Multiple-vibrational-mode model for fiber-optic Raman gain spectrum and response function. *J. Opt. Soc. Am. B* **19**, 2886–2892 (2002).

[25] Qi, B., Zhu, W., Qian, L. & Lo, H.-K. Feasibility of quantum key distribution through a dense wavelength division multiplexing network. *New J. Phys.* **12**, 103042 (2010).

[26] Ferreira da Silva, T., Xavier, G. B., Temporão, G. P. & von der Weid, J. P. Impact of Raman scattered noise from multiple telecom channels on fiber-optic quantum key distribution systems. *J. Lightwave Technol.* **32**, 2332–2339 (2014).

[27] Ivan, J. S., Sabapathy, K. K. & Simon, R. Operator-sum representation for bosonic Gaussian channels. *Phys. Rev. A* **84**, 042311 (2011).

[30] Xavier, G. et al. Experimental polarization encoded quantum key distribution over optical fibres with real-time continuous birefringence compensation. *New J. Phys.* **11**, 045015 (2009).